SCIENCE CHINA
Physics, Mechanics & Astronomy

• Article •

August 2025 Vol. 68 No. 8: 287511
https://doi.org/10.1007/s11433-025-2677-x

3*d* flat bands and coupled 4*f* moments in the kagome-honeycomb permanent magnet Sm_2Co_{17}

Hao Zheng[1,2], Zhiguang Xiao[1,2], Ze Pan[1,2], Guowei Yang[1,2], Yonghao Liu[1], Jianzhou Bian[1], Yi Wu[1,2], Teng Hua[1,2], Jiawen Zhang[1,2], Jiayi Lu[1], Jiong Li[3], Tulai Sun[4], Yu Song[1,2], Ruihua He[5], J. Larrea Jiménez[6], Guanghan Cao[1,7,8], Huiqiu Yuan[1,2,8], Yuanfeng Xu[1,2], Yi Yin[1,8], Ming Shi[1,2*], Chao Cao[1,2*], and Yang Liu[1,2,8*]

[1] *School of Physics, Zhejiang University, Hangzhou 310058, China*
[2] *Center for Correlated Matter, Zhejiang University, Hangzhou 310058, China*
[3] *Shanghai Synchrotron Radiation Facility, Shanghai Advanced Research Institute, Chinese Academy of Sciences, Shanghai 201204, China*
[4] *Center for Electron Microscopy, Zhejiang University of Technology, Hangzhou 310014, China*
[5] *Key Laboratory for Quantum Materials of Zhejiang Province, Department of Physics, and Zhejiang Institute for Advanced Light Source, Westlake University, Hangzhou 310058, China*
[6] *Laboratory for Quantum Matter under Extreme Conditions, Institute of Physics, University of São Paulo, São Paulo 05508-090, Brazil*
[7] *Interdisciplinary Center for Quantum Information, and State Key Laboratory of Silicon and Advanced Semiconductor Materials, Zhejiang University, Hangzhou 310058, China*
[8] *Collaborative Innovation Center of Advanced Microstructures, Nanjing University, Nanjing 210093, China*

Received February 17, 2025; accepted April 23, 2025; published online June 24, 2025

Rare earth permanent magnets (REPMs) with both localized moments and itinerant conduction bands are not only important for fundamental research but also have significant technological applications. In particular, Sm_2Co_{17} is a prototypical high-temperture REPM, where the Co atoms form a kagome-honeycomb stacked lattice. Here we report the synthesis of epitaxial Sm_2Co_{17} films using molecular beam epitaxy and measurements of their momentum-resolved electronic structure from *in-situ* angle-resolved photoemission spectroscopy. Our results unveil two flat bands from Co 3*d* orbitals near the Fermi level (E_F), one at ~ -300 meV and another right at E_F, which arise from orbital-selective destructive interference and strong electron correlations, respectively. In addition, our results reveal that Sm 4*f* states are far away from E_F (hence mostly localized) and exhibit an anomalous temperature dependence, caused by the 3*d*-4*f* magnetic coupling. Our findings provide direct spectroscopic insights to understand the strong uniaxial ferromagnetism in Sm_2Co_{17} (and REPMs alike). Our work also opens avenues to explore flat-band physics near E_F and emergent phenomena in correlated kagome-honeycomb lattices.

kagome lattice, flat bands, rare-earth permanent magnet, molecular beam epitaxy, angle-resolved photoemission spectroscopy

PACS number(s): 71.20.Be, 71.20.Eh, 73.22.-f, 75.50.Ww, 81.15.-z

Citation: H. Zheng, Z. Xiao, Z. Pan, G. Yang, Y. Liu, J. Bian, Y. Wu, T. Hua, J. Zhang, J. Lu, J. Li, T. Sun, Y. Song, R. He, J. L. Jiménez, G. Cao, H. Yuan, Y. Xu, Y. Yin, M. Shi, C. Cao, and Y. Liu, 3*d* flat bands and coupled 4*f* moments in the kagome-honeycomb permanent magnet Sm_2Co_{17}, Sci. China-Phys. Mech. Astron. **68**, 287511 (2025), https://doi.org/10.1007/s11433-025-2677-x

*Corresponding authors (Ming Shi, email: shi20001231@zju.edu.cn; Chao Cao, email: ccao@zju.edu.cn; Yang Liu, email: yangliuphys@zju.edu.cn)

1 Introduction

Rare-earth permanent magnets (REPMs), which are intermetallic compounds composed of rare earth (R) and transition metal (T) elements, are extensively utilized in the automotive, data storage, electric power, and medical imaging industries. The key feature driving their widespread application is their strong uniaxial ferromagnetism (FM), which remains robust against demagnetization. Significant efforts have been dedicated to elucidating the fundamental mechanisms underpinning the robust FM in REPMs [1-7], aiming to design and engineer superior REPM materials. While the strong uniaxial FM is typically explained by the magnetic exchange interactions of the 3d and 4f sublattices [8,9], particularly the 3d-3d and 3d-4f interactions, the different types of exchange interactions are expected due to the localized or itinerant nature of 4f/3d electrons. Therefore, it is crucial to reveal their energy positions relative to the Fermi level (E_F) and momentum dispersions for a fundamental understanding of REPMs. However, direct measurements of their momentum-resolved electronic structures have remained elusive up to now.

Among REPMs, Sm_2Co_{17} stands out due to their exceptionally strong FM and very high Curie temperatures (T_c) [2]. Interestingly, it belongs to a large family of binary compounds R_xT_y (x:y being 1:5, 2:17, 1:2, etc.), which feature kagome layers composed of transition metal atoms T (see Figure 1(a-c)). Recently, kagome-based materials have generated widespread interest in physics and material science [10, 11], owing to a variety of many-body phases including superconductivity [12-14], FM [15-18], spin/charge density waves [19-22], Wigner crystal [23], and fractional quantum Hall effect [24-26]. In particular, destructive interference of electronic wave functions in the kagome lattice can give rise to flat bands with a high density of states (DOS), as recently observed by angle-resolved photoemission spectroscopy (ARPES) [27-35]. However, in most cases, the flat bands are far away from E_F and they do not make significant contributions to the physical properties. If the flat bands are close to the E_F, they can be favorable for the formation of flat-band FM [15, 16]. In Sm_2Co_{17}, the kagome Co layers are sandwiched by honeycomb Co layers, and symmetry-protected flat bands were predicted in such a kagome-honeycomb lattice [36-38], motivating the spectroscopic detection of these flat bands and the exploration of their connection to the robust FM.

A typical method for measuring the momentum-dependent electronic structure is ARPES. However, this is challenging for REPMs, as ARPES measurements typically require large single crystals with natural cleavage planes and minimal residual magnetic field. For Sm_2Co_{17}, single crystals are very difficult to synthesize [39], hampering in-depth understanding of its intrinsic properties. Here, we successfully overcome these experimental obstacles by combining thin film growth via molecular beam epitaxy (MBE) with *in-situ* ARPES measurements [40], thereby obtaining for the first time the momentum-resolved electronic structure of a prototypical REPM Sm_2Co_{17}. Our work paves the way for a fundamental understanding of the strong uniaxial ferromagnetism in Sm_2Co_{17} (and other REPMs) from an electronic structure perspective and represents a step forward to search for flat bands beyond the simple kagome lattice [36,37]. Our synthesis of epitaxial Sm_2Co_{17} films also opens up opportunites to explore thin-film applications based on REPMs.

2 Experimental and calculational methods

The epitaxial Sm_2Co_{17} films were grown on Al_2O_3(0001) substrates, modified from a previous growth method [41]. The base pressure of the MBE chamber is better than 1×10^{-10} mbar. The evaporations of Sm and Co were achieved using effusion cells, whose deposition rates were set to approximately ~0.8 Å min^{-1} for Sm and ~1.4 Å min^{-1} for Co, respectively, as determined by a quartz crystal monitor. Before growth, Al_2O_3 substrates were heated up to 650°C in ultrahigh vacuum for 30 min. We found it helpful to first grow a thin Co buffer layer at 120°C before the actual growth of Sm_2Co_{17}. The substrates were then heated to 400°C for growing Sm_2Co_{17} films. The growth of Sm_2Co_{17} films was monitored by *in-situ* reflection high-energy electron diffraction (RHEED). After growth, the Sm_2Co_{17} films (typically 20 nm) were transferred under an ultrahigh vacuum to a lab-based ARPES system equipped with a helium lamp for *in-situ* ARPES measurements. The sample temperature was kept at ~ 6 K during all measurements unless noted otherwise. All ARPES data were taken with the He Iα (21.2 eV) or He II (40.8 eV) photons. The typical energy and momentum resolution is ~12 meV and ~0.01 Å^{-1}, respectively.

Density functional theory (DFT) calculations were performed using the Vienna *Ab initio* Simulation Package (VASP) [42, 43], incorporating the Perdew-Burke-Ernzerhof (PBE) generalized gradient approximation (GGA) [44] for the exchange-correlation functional. To model the ferromagnetic state, Sm 4f electrons were treated as valence electrons with a Hubbard interaction U = 7.0 eV and Hund's coupling J = 1.0 eV, as is commonly adopted for Sm-based systems. A linear interpolation double-counting (DC) scheme between fully localized limit (FLL) DC and around-mean-field (AMF) DC [45, 46], which minimizes the total energy was chosen to give a reasonable magnetic moment of Sm. For Co 3d electrons, we found that U = J = 0

gave the best agreement with our experimental results (see Supplementary Information for details). To achieve a quantitative match with experiment, we applied a bandwidth renormalization (reduction) factor of ~ 1.7, which is not uncommon in strongly correlated 3*d*-electron systems as DFT calculations tend to overestimate the bandwidth [47-50].

The structure of Sm_2Co_{17} films was examined using *ex-situ* high-angle annular dark-field scanning transmission electron microscopy (HAADF-STEM) and X-ray diffraction (XRD). HAADF-STEM imaging was carried out on a state-of-the-art spherical-aberration-corrected transmission electron microscope. Synchrotron XRD and X-ray absorption spectroscopy (XAS) were performed at beamlines BL02U2, BL07U, and BL11B of the Shanghai Synchrotron Radiation Facility (SSRF). Magnetic properties were studied with a SQUID magnetometer at low temperatures, subtracting the substrate signal. To minimize contributions from the Co buffer, these *ex-situ* measurements were done on thicker Sm_2Co_{17} layers (typically 100 nm) with a very thin or no Co buffer.

3 Results

3.1 Characterization of Sm_2Co_{17} films

The fundamental building block of R_xT_y compounds is the hexagonal RT_5 structure, as illustrated in Figure 1(a) (taking $SmCo_5$ as an example). This structure consists of alternating $SmCo_2$ and Co layers stacked along the *c* axis. Within the Co layer, the Co atoms form a pure kagome lattice without interstitial atoms, while in the $SmCo_2$ layer, Sm and Co atoms are arranged in triangular and honeycomb lattices, respectively. By periodically replacing one-third of the Sm atoms in the $SmCo_2$ layer with a Co-Co dimer (green balls in Figure 1(b) and (c)), the rhombohedral phase of Sm_2Co_{17} can be obtained. Hence, the Sm_2Co_{17} lattice can be viewed as a weakly distorted version of the basic $SmCo_5$ lattice, with an enlarged unit cell of $a^* \approx \sqrt{3}\,a$ and $c^* \approx 3\,c$, where a^* and c^* (a and c) are the lattice constants of Sm_2Co_{17} ($SmCo_5$). Notably, the kagome and honeycomb Co layers remain intact in the Sm_2Co_{17} structure (yellow and blue balls in Figure 1(b) and (c)).

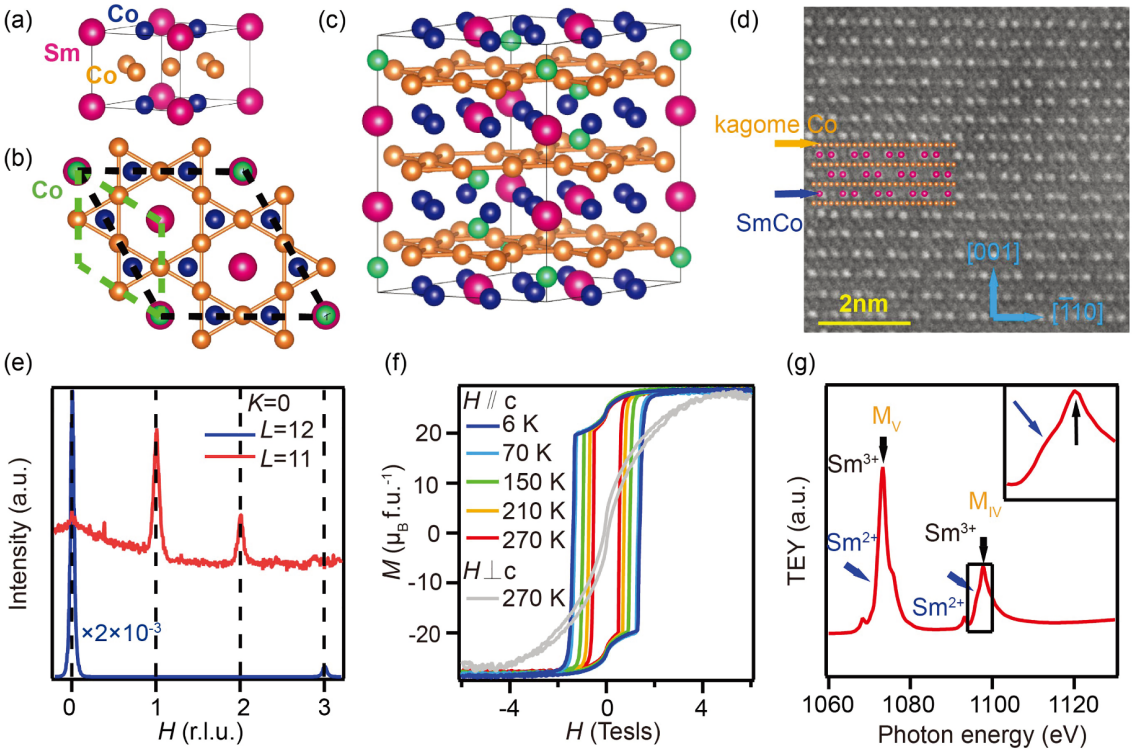

Figure 1 (Color online) (a) The primitive cell of $SmCo_5$. (b) Top view of the unit cell of Sm_2Co_{17}. (c) The conventional cell of rhombohedral Sm_2Co_{17}. The yellow and blue balls in (a-c) indicate Co atoms in the kagome and honeycomb layers, respectively. (d) HAADF-STEM image of a Sm_2Co_{17} film. Yellow and blue arrows indicate the kagome Co and SmCo layers. (e) Synchrotron XRD scans along H at two L values (note the different multiplication factors). (f) The magnetization M as a function of field H at different temperatures for fields parallel and perpendicular to the *c* axis. (g) XAS result of a thick Sm_2Co_{17} film near the Sm M edge, obtained from total electron yield (TEY). The inset shows a zoom-in view near the M_{IV} edge, highlighting a very weak Sm^{2+} component. The Sm^{3+} and Sm^{2+} components are marked by black and blue arrows, respectively.

We successfully grew high-quality Sm_2Co_{17} films using MBE (See Supplementary Information Figure S1 for more details). The sample quality is verified by the atomic-resolution images obtained via HAADF-STEM (Figure 1(d)) and the sharp peaks from synchrotron XRD (Figure 1(e)). Specifically, since one third of Sm atoms in Sm_2Co_{17} is replaced periodically with a Co-Co dimer compared with $SmCo_5$, the Sm atoms in the SmCo layer exhibit a ×3 periodicity along [$\bar{1}$10], which can be clearly identified in Figure 1(d) as two bright spots and one weak spot. The XRD result in Figure 1(e), where the H, K, and L directions are defined with respect to the bulk Sm_2Co_{17} lattice, shows that the superstructure peaks exclusively associated with Sm_2Co_{17}, e.g., (H, K, L)=(1, 0, 11), can be observed, although they are nearly three orders of magnitude weaker than the dominant peaks expected from ideal $SmCo_5$, e.g., (H, K, L)=(0, 0, 12). This indicates that the superstructure distortion from $SmCo_5$ to Sm_2Co_{17} is weak but clearly discernible.

The magnetization as a function of applied field (M-H curves) is summarized in Figure 1(f), clearly showing ferromagnetic behavior with pronounced hysteresis loops. When the field is aligned along the c axis (the easy axis), the saturation moment remains nearly unchanged up to 270 K, consistent with a high Curie temperature (T_C). In contrast, the coercive field (H_c) is strongly temperature-dependent (Figure 1(f) and Supplementary Information Figure S1): For instance, H_c increases from ~0.5 T at 270 K to ~1.4 T at 6 K. The strong magnetocrystalline anisotropy (MCA), which is crucial for rare-earth permanent magnet (REPM) applications, is evident from the M-H response measured with the field perpendicular to the c axis (Figure 1(f)), where the moment remains unsaturated even under a field of ~4 T and the hysteresis is significantly reduced. Therefore, our magnetic measurements of single-crystal thin films confirm the strong MCA expected in Sm_2Co_{17} and also reveal its pronounced temperature dependence, which can be related to the anomalous temperature evolution of 4f states (see sect. 3.4). Finally, measurements from XAS (Figure 1(g)) show dominant contributions from Sm^{3+} (strong peaks marked by black arrows), and very weak Sm^{2+} components (shoulder structures marked by blue arrows).

An advantage of MBE growth is the ability to control the surface termination. Figure 2 compares the energy distribution curves (EDCs) from photoemission measurements for kagome Co and SmCo terminated surfaces. For the kagome Co termination, two flat bands at −5.6 and −8 eV (indicated by black arrows in Figure 2(c)) can be clearly observed. These features can be attributed to bulk 4f states associated with Sm^{3+} ($4f^5$), consistent with previous studies on Sm-based compounds [51-53]. In contrast, for the SmCo termination, these 4f states shift downward by approximately 0.4 eV (red arrows), likely due to a surface core-level shift [51,54,55], while an intense peak emerges near −5 eV (green arrow), possibly a pure surface component [55, 56]. Moreover, the valence bands from −2 eV to E_F are obviously stronger for the kagome Co termination, as they predominantly originate from Co 3d electrons (see below).

3.2 Fermi surface and flat bands on kagome Co termination

Figure 3(a) presents constant-energy k_x-k_y maps on the

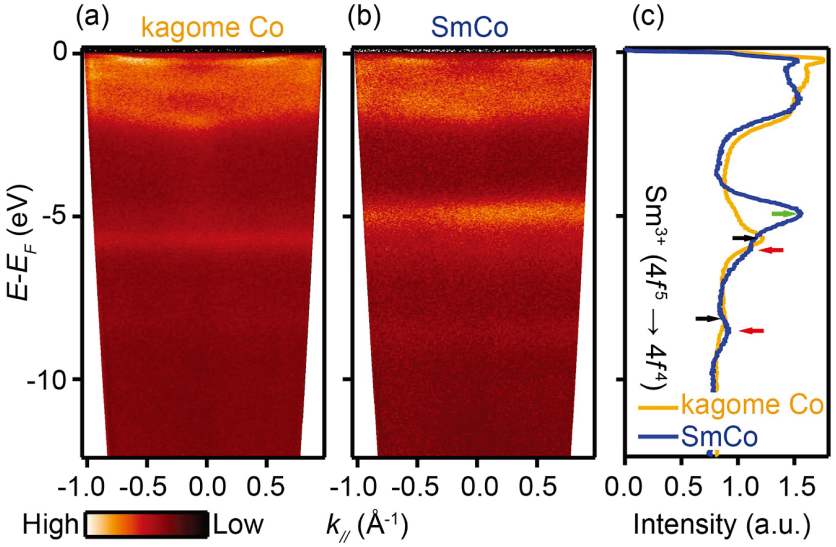

Figure 2 (Color online) (a), (b) Large-scale ARPES spectra of kagome Co terminated surface (a) and SmCo terminated surface (b) using 40.8 eV photons. (c) The corresponding momentum-integrated EDCs of two terminations. The black and red arrows indicate the bulk and surface-shifted 4f peaks, while the green arrow indicates a surface 4f peak on the SmCo termination.

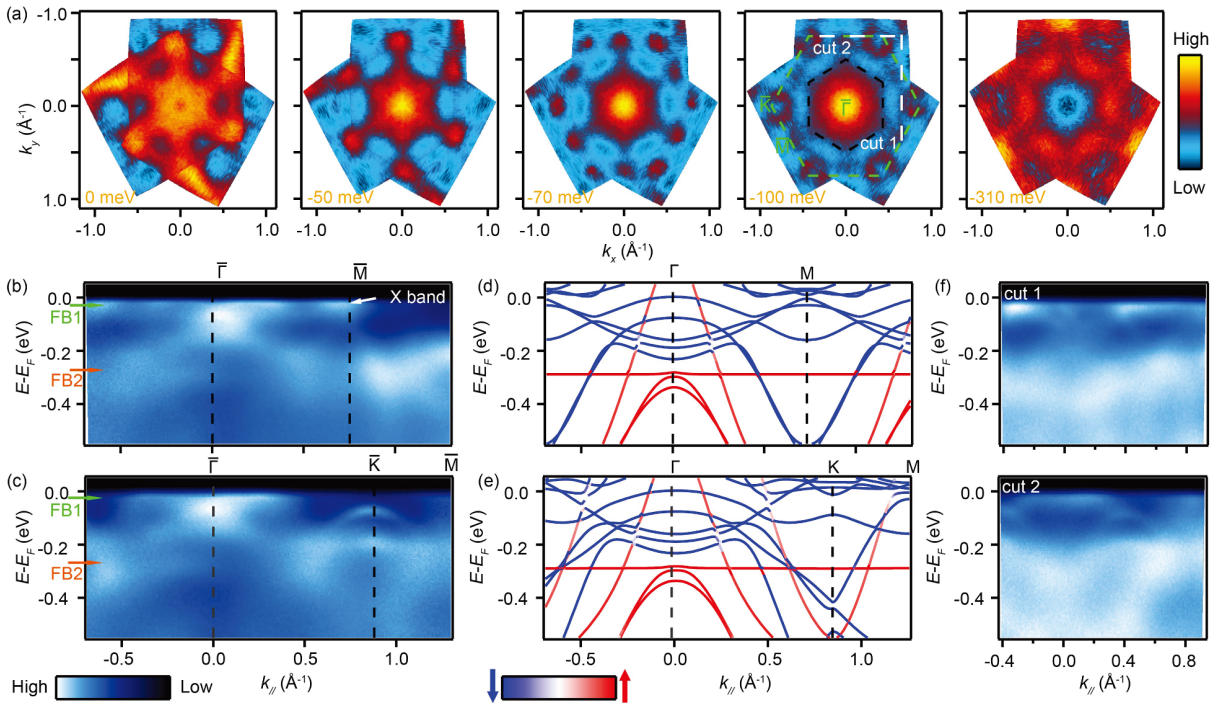

Figure 3 (Color online) Electronic structure for kagome Co terminated surface. (a) Constant energy k_x-k_y maps at various energies. The original data, covering more than half of the surface BZ, were symmetrized according to the bulk C_3 symmetry to yield these maps. Green and black dashed hexagons on the −100 meV map indicate the surface BZ's of $SmCo_5$ and Sm_2Co_{17}, respectively. (b), (c) Experimental energy-momentum cuts along $\bar{\Gamma}$-$\bar{M}$ (b) and $\bar{\Gamma}$-$\bar{K}$-$\bar{M}$ (c). (d), (e) Spin-resolved band structure from DFT+U along Γ-M (d) and Γ-K-M (e), for comparison with (b), (c). The red and blue curves indicate majority-spin and minority-spin bands, respectively. (f) Experimental energy-momentum cuts along two directions labeled in the −100 meV map in (a).

kagome Co terminated surface, acquired from ARPES using 21.2 eV photons. This corresponds to $k_z \sim 4\pi/c$ based on an estimated inner potential $V_0 = 19.6$ eV, determined by matching the ARPES data taken with both 21.2 and 40.8 eV photons to the calculations (see Supplementary Information Figure S2 for data taken by 40.8 eV photons). Notably, the dominant features in these maps follow the surface Brillouin zone (BZ) of the Co kagome layer, which is the same as $SmCo_5$ (green dashed hexagon at $E = -100$ meV), rather than the smaller BZ of Sm_2Co_{17} (black dashed hexagon). For instance, at $E = -100$ meV, circular hole pockets are clearly observed at the $\bar{K}$ points of the $SmCo_5$ BZ. This whole band at $\bar{K}$ is evident in the energy-momentum cut of Figure 3(c), where the band maximum is located near −70 meV. Meanwhile, an electron pocket centered at $\bar{M}$ emerges around −70 meV (Figure 3(a)) and expands upon approaching E_F, corresponding to the upper branch of an X-shaped band at $\bar{M}$ (white arrow in Figure 3(b)). The fact that the measured bands follow the surface BZ of the Co kagome layer (or $SmCo_5$) indicates that the surface-sensitive ARPES spectra are mostly contributed by electronic states residing on the Co kagome layer and are therefore not sensitive to the weak lattice distortion of the $SmCo_2$ layer in Sm_2Co_{17}. Hence, for simplicity, we compare our ARPES data with the simpler band structure of $SmCo_5$, as shown in Figure 3(d) and (e). Indeed, most of the spectral features can be reasonably captured by this simplified calculation. By contrast, many band features predicted from the Sm_2Co_{17} calculation are not observed experimentally (see Supplementary Information Figure S3), further validating our comparison with the simplified band structure of $SmCo_5$ that ignores the weak distortion in the $SmCo_2$ layer.

In Figure 3(a), a broad pocket centered at $\bar{\Gamma}$ is observed at E_F ($E = 0$), extending over a large momentum range. This feature corresponds to a nearly dispersionless band, labeled FB1 in Figure 3(b) and (c). In addition, another flat band (FB2) appears around −300 meV, exhibiting only slight dispersion (see also the second-derivative data in Supplementary Information Figure S4 for a clearer presentation). Figure 3(f) shows two additional energy–momentum cuts, demonstrating that both FB1 and FB2 persist over a wide momentum range. Additionally, our *ex-situ* STM measurements (see Supplementary Information Figure S5) also demonstrate the existence of FB2, shown as an robust peak at ∼ −300 meV in STS spectra.

Figure 3(d) and (e) depict the spin-resolved band structure for ferromagnetic $SmCo_5$, calculated via DFT including Hubbard U and Hund's coupling J (DFT+U) (see Supporting Information for more details). The calculations indicate that the Sm valence is close to Sm^{3+} ($4f^5$), and correspond-

ingly the 4f multiplet lies several eV's below E_F, consistent with our XAS and photoemission results (Figures 1(g) and 2). Moreover, the valence bands near E_F predominantly originate from Co 3d electrons and exhibit large spin splitting (Supplementary Information Figure S6). The majority-spin bands (red) are almost fully occupied below E_F, whereas the minority-spin bands (blue) dominate near E_F. The essential experimental features near E_F are reasonably reproduced (compare Figure 3(b) and (c) and 3(d) and (e)). Interestingly, the calculations also reveal a nearly non-dispersive band at ~ -300 meV, which is consistent with the FB2 band observed experimentally.

The FB1 band at E_F is not adequately captured by the DFT+U calculations. While it is tempting to attribute this band to Sm 4f states, our experimental results are inconsistent with such a scenario: The photoemission intensity of FB1 strongly decreases when using 40.8 eV photons (Supplementary Information Figure S7), whereas the photoemission cross section for 4f electrons should be enhanced under this photon energy. This indicates that FB1 is predominantly derived from Co 3d orbitals rather than Sm 4f electrons. This is also consistent with the Sm valence being close to 3+ below (see sect. 3.4), where the Sm 4f states near E_F corresponding to Sm^{2+} should be weak. Therefore, the FB1 is most likely caused by the strong correlation effects in a multi-orbital 3d system, due to a combination of Hubbard interaction U and Hund's coupling J [57,58]. Such correlation effects can lead to orbital-selective band renormalization, an accurate description of which is beyond the scope of standard DFT methods [59,60].

3.3 Destructive interference in a kagome-honeycomb lattice

Figure 4(a) and (b) shows the orbital- and layer-resolved band structure of $SmCo_5$ obtained from DFT+U calculations (see also Supplementary Information Figure S8). Here, the orbitals were grouped into d_{xz}+d_{yz} and d_{xy}+$d_{x^2-y^2}$+d_{z^2}, respectively, based on the wavefunction symmetry and orbital-selective destructive interference discussed in ref. [38]. They demonstrate that the flat band near -300 meV (FB2) originates from Co d_{xz} and d_{yz} orbitals, with contributions from both the kagome and honeycomb layers. By contrast, the minority-spin bands at E_F (corresponding to FB1) arise mainly from d_{xy} and $d_{x^2-y^2}$ orbitals located in the kagome layer. This naturally explains why, on the SmCo terminated surface (Figure 4(d)), the FB1 band near E_F is much weaker compared with the kagome Co termination (Figure 4(c)), whereas the FB2 band remains strong, thanks to the surface sensitivity of ARPES measurements. Moreover, the layer-resolved (and orbital-integrated) DFT+U calculations in Figure 4(e) and (f) can reasonably reproduce the observed spectral features and their termination dependence (comparing Figure 4(e) and (f) with Figure 4(c) and (d)).

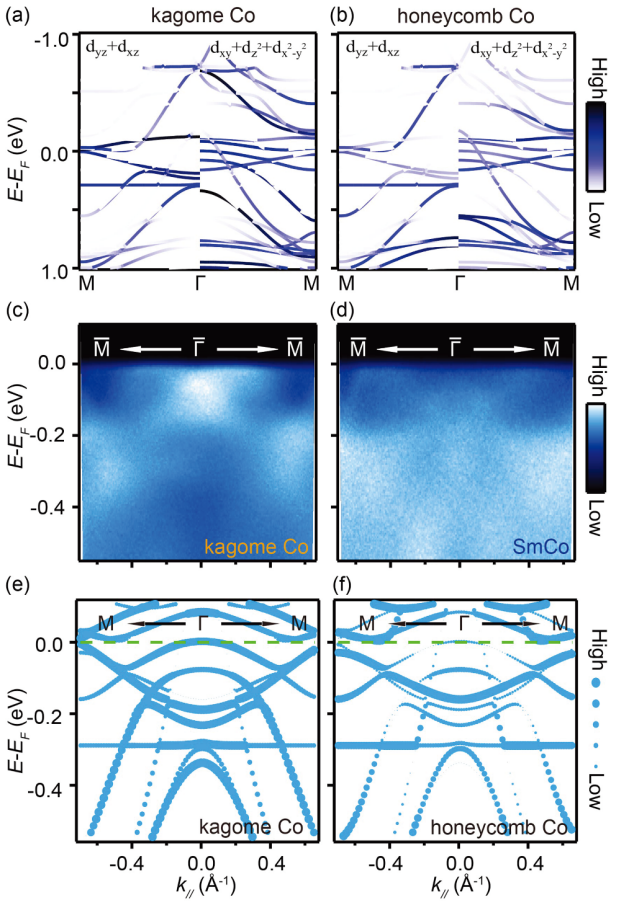

Figure 4 (Color online) (a), (b) Orbital-resolved DFT+U band structure (left: d_{xz}+d_{yz}. right: d_{xy}+d_{z^2}+$d_{x^2-y^2}$) projected from kagome Co (a) and honeycomb Co (b) layers. (c), (d) ARPES spectra near E_F corresponding to kagome Co (c) and SmCo (d) terminations. (e), (f) Orbital-integrated layer-resolved band structure from the kagome Co (e) and honeycomb Co (f) layers, for comparison with (c) and (d). The color bars are shown on the right.

The very flat band at ~ -300 meV (Figure 3(d) and (e)) and its spatial extension into the honeycomb layer (Figure 4(a) and (b)) are noteworthy, since interlayer hopping and multiorbital mixing often destroy flat bands in kagome lattices. Here, the flat band arises from orbital-selective destructive interference in the kagome-honeycomb stacked lattice, as theoretically proposed in refs. [36,38]: The lattice symmetry effectively decouples the d_{xz} and d_{yz} orbitals from other orbitals at $k_z = 0$, leading to destructive interference for both intralayer hopping within the kagome layer and interlayer hopping between the kagome and honeycomb layers. This interplay results in a symmetry-enforced flat band at $k_z = 0$, namely FB2. Our calculations further indicate that this flat band persists over a considerable range in k_z (Supplementary Information Figure S9).

3.4 4*f* states and temperature evolution

The 4*f* electrons play an important role in generating the large MCA in REPMs [61-63]: The crystal electric field (CEF) experienced by 4*f* electrons produces strongly anisotropic 4*f* moments, which couple to 3*d* moments, leading to large coercive fields and resistance against demagnetization. Typically, 4*f* electrons are regarded as stable, with negligible valence mixing. However, Sm-based materials often exhibit valence fluctuations between Sm^{3+} and Sm^{2+}, as exemplified by SmB_6 [64-66], where the average Sm valence is close to 2.6. In Sm_2Co_{17}, both XAS measurements and DFT calculations indicate that the Sm valence remains predominantly 3^+, albeit with small 2^+ component. Figure 5(a) displays the temperature evolution of the 4*f* states associated with Sm^{3+}, whose intensity (proportional to the Sm^{3+} component) gradually increases upon cooling. This phenomenon is corroborated by additional measurements under repeated temperature cycling on different samples (Supplementary Information Figure S11). Moreover, our ARPES data reveal reduction of spectral intensities near −0.5 and −1.5 eV upon cooling, which could indicate either a direct response of the Co 3*d* states due to the 3*d*-4*f* coupling or a reduction in the

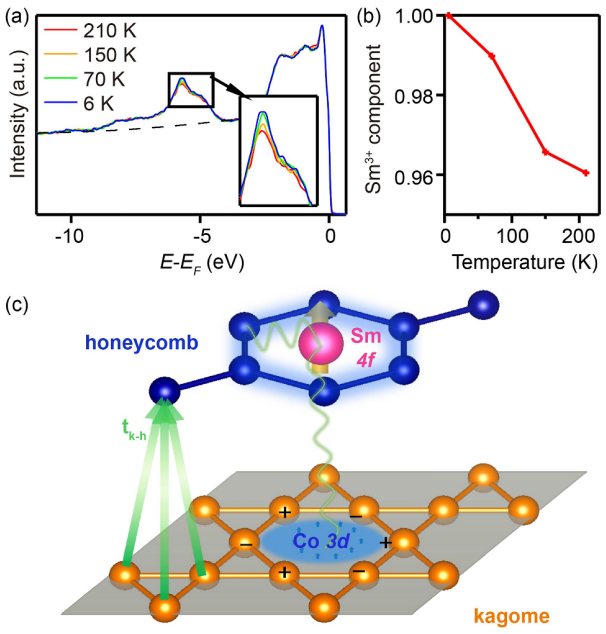

Figure 5 (Color online) (a) Temperature evolution of momentum-integrated EDCs. The inset shows a zoom-in view of the Sm^{3+} 4*f* states. (b) The Sm^{3+} component extracted from (a) and normalized to its value at 6 K. (c) A cartoon illustrating the 3*d*-3*d* and 3*d*-4*f* magnetic interactions. The 3*d*-3*d* interaction stems from itinerant 3*d* bands, which develop flat bands from destructive interferences, for both intralayer hopping within the kagome layer (light blue) and interlayer hopping between the kagome and honeycomb layers (green arrows). The 3*d*-4*f* interaction, indicated by grey wavy lines, is realized through mostly localized 4*f* electrons with suppressed valence fluctuation and contributes to the large MCA.

Sm^{2+} component. Future temperature-dependent resonant photoemission measurements, to be carried out in synchrotron facilities with tunable photon energies, will be crucial for distinguishing these two scenarios.

To quantify the temperature-dependent valence change, we integrated the intensity of the Sm^{3+} 4*f* peak (from −10 to −4 eV) after background subtraction and normalized it to its value at 6 K (Figure 5(b)). The analysis indicates a small valence increase of approximately 0.04 from 210 to 6 K, which is difficult to resolve in XAS measurements. Such a low-temperature increase in Sm valence is rather unusual, contrasting with well-known mixed-valent Sm systems [64, 67], where Sm valence typically decreases toward Sm^{2+} at low temperature due to enhanced 4*f* itineracy. Such anomalous temperature evolution could be attributed to the magnetic coupling between Sm 4*f* moments and Co 3*d* bands, which we shall discuss below.

4 Discussion

The flat bands observed near E_F, arising from destructive interference in the kagome-honeycomb lattice (FB2) and from strong 3*d* correlation effects (FB1), contribute to an enhanced DOS that can promote itinerant FM in Sm_2Co_{17}. This mechanism could also apply to other RCo_5 and R_2Co_{17} compounds, providing a natural explanation for their common ferromagnetic behavior [2, 4]. According to calculations [38, 68], the FB2 band is highly tunable under pressure or strain. Interestingly, experiments on YCo_5 (which lacks 4*f* electrons) have revealed a marked magnetoelastic lattice collapse under pressure [69], attributed to a Lifshitz transition when FB2 crosses E_F [38, 68]. In Sm_2Co_{17}, the FB1 flat band near E_F persists over a large k_z range (Supplementary Information Figures S2 and S9). Such spin-polarized flat bands at E_F open avenues for exploring emergent phenomena, e.g., high-temperature fractional quantum Hall effects [24-26].

The robust uniaxial FM in REPMs is often explained through 3*d*-3*d* and 3*d*-4*f* magnetic interactions. Our momentum-resolved measurements directly verify the itinerant (localized) character of the 3*d* (4*f*) electrons underlying these interactions, as illustrated schematically in Figure 5(c): The 3*d*-3*d* coupling stems from itinerant Co 3*d* bands near E_F and dominates the FM with a large band splitting of ~ 1 eV (Supplementary Information Figure S6). In contrast, Sm 4*f* electrons remain mostly localized, and the exchange coupling *J* of the 3*d*-4*f* interaction, estimated from DFT+*U* calculations, is on the order of a few tens of meV—much smaller than the 3*d*-3*d* interaction. Furthermore, our DFT+*U* results indicate that the 4*f* spin moments align parallel to the minority-spin direction of the 3*d* electrons (see

Supplementary Information Table S1), whereas the $4f$ orbital moments are antiparallel to (and larger than) their spin moments. Hence, the net moments of Sm $4f$ and Co $3d$ electrons are parallel and ferromagnetically coupled along the c-axis. These findings naturally account for the strong FM observed in Sm_2Co_{17} [61]. Previous studies have proposed that the $3d$-$4f$ interaction is most likely mediated by the small amount of Sm $5d$ states near E_F [8], which is supported by our calculations in Supplementary Information Figure S6. In addition, because FB1 has a clear overlap with these $5d$ states, its nearly flat dispersion with large DOS can further reinforce the indirect $3d$-$4f$ exchange and thus help boost the uniaxial ferromagnetism.

The $3d$-$4f$ interaction is important for the large MCA in REPMs and is likely the cause of the anomalous temperature evolution of the Sm valence. Specifically, the enhanced Sm^{3+} component at low temperatures in Sm_2Co_{17} could be attributed to its strong ferromagnetic order, which competes with the $4f$ delocalization process driven by Sm valence fluctuations, thereby suppressing itinerant (and nonmagnetic) Sm^{2+} components. This scenario is analogous to the well-known competition between magnetic order and Kondo screening in Ce- and Yb-based Kondo systems [70-73]. Our findings thus suggest that strong valence fluctuations (or the Kondo effect) could undermine the robust FM (and consequently the performance of REPMs), in agreement with recent theoretical studies on Ce-based REPMs [74, 75]. Interestingly, the rise in the Sm^{3+} component coincides with a pronounced increase in the coercive field H_c at low temperature (Figure 1(f) and Supplementary Information Figure S1(d)). It would therefore be interesting to investigate how this valence change can be connected to the enhanced H_c at low temperatures [62].

5 Conclusion

In summary, we have successfully grown epitaxial Sm_2Co_{17} films by MBE and revealed, for the first time, the the layer- and momentum-dependent electronic structure for a typical REPM. Our results unveil that the Co $3d$ electrons form flat bands near E_F, one at ~ -300 meV and another right at E_F, which arise from the orbital-selective destructive interference in a kagome-honeycomb lattice and correlation effects, respectively. Our work further reveals that Sm^{3+} $4f$ states are far away from E_F and exhibit an anomalous temperature evolution, due to the $3d$-$4f$ interaction and competition with strong FM. These findings can be reasonably captured by theoretical calculations, thereby paving the way for a fundamental understanding of REPMs. The spectroscopic insight also hints on alternative approaches to search for high-performance REPMs, through judicious design/engineering of crystal structures and associated flat bands. Finally, our results also suggest new routes to explore emergent phenomena associated with flat bands near E_F [60, 76, 77], by generating destructive interference in kagome-honeycomb lattices in combination with strong correlation effects.

This work was supported by the National Key Research and Development Program of China (Grant Nos. 2022YFA1402200, 2023YFA1406303 and 2022YFA1403202), the National Natural Science Foundation of China (Grant Nos. 12174331, 12350710785 and 12274353), the Key Research and Development Program of Zhejiang Province, China (Grant No. 2021C01002), the State Key Project of Zhejiang Province (Grant No. LZ22A040007), Zhejiang Provincial Natural Science Foundation of China (Grant Nos. LGG22E020006 and LDG25A040001), Centro Nacional de Desenvolvimento Científico e Tecnológico (CNPq) (Grant No. 404312/2024-1) and São Paulo Research Foundation (FAPESP) (Garnt No. 2018/08845-3). We thank Prof. Frank Steglich, Prof. Zhentao Wang, Prof. Zheng Liu, Prof. Michael Smidman, Prof. Jiaying Jin, Prof. Yanwu Xie, Prof. Zhicheng Zhong, Prof. Xin Lu, Prof. Jiefeng Cao, Dr. Bodry Tegomo Chiogo, Dr. Ruiwen Xie, Dr. Shuaishuai Yin, Dr. Ge Ye and Ms. Xueshan Cao for discussions and help on experiments.

Conflict of interest The authors declare that they have no conflict of interest.

Supporting Information

The supporting information is available online at http://phys.scichina.com and https://link.springer.com. The supporting materials are published as submitted, without typesetting or editing. The responsibility for scientific accuracy and content remains entirely with the authors.

1 J. F. Herbst, Rev. Mod. Phys. **63**, 819 (1991).
2 K. H. J. Buschow, Rep. Prog. Phys. **40**, 1179 (1977).
3 J. M. D. Coey, IEEE Trans. Magn. **47**, 4671 (2011).
4 O. Gutfleisch, M. A. Willard, E. Bräck, C. H. Chen, S. G. Sankar, and J. P. Liu, Adv. Mater. **23**, 821 (2011).
5 H. Nakamura, Scripta Mater. **154**, 273 (2018).
6 C. Fang, Z. Yan, X. J. Zhang, J. H. Xiao, F. Wang, and X. H. Xu, Sci. China-Phys. Mech. Astron. **68**, 247512 (2025).
7 D. Liu, J. Xiong, L. Wang, X. Zheng, X. Ming, J. Jin, J. Hao, H. Bai, Z. Li, T. Zhao, et al., Sci. China-Phys. Mech. Astron. **68**, 227512 (2025).
8 I. A. Campbell, J. Phys. F-Met. Phys. **2**, L47 (1972).
9 M. S. S. Brooks, T. Gasche, S. Auluck, L. Nordström, L. Severin, J. Trygg, and B. Johansson, J. Appl. Phys. **70**, 5972 (1991).
10 J. X. Yin, B. Lian, and M. Z. Hasan, Nature **612**, 647 (2022).
11 Y. Wang, H. Wu, G. T. McCandless, J. Y. Chan, and M. N. Ali, Nat. Rev. Phys. **5**, 635 (2023).
12 W. H. Ko, P. A. Lee, and X. G. Wen, Phys. Rev. B **79**, 214502 (2009).
13 S. L. Yu, and J. X. Li, Phys. Rev. B **85**, 144402 (2012).
14 B. R. Ortiz, S. M. L. Teicher, Y. Hu, J. L. Zuo, P. M. Sarte, E. C. Schueller, A. M. M. Abeykoon, M. J. Krogstad, S. Rosenkranz, R. Osborn, et al., Phys. Rev. Lett. **125**, 247002 (2020).
15 A. Mielke, J. Phys. A-Math. Gen. **24**, L73 (1991).
16 H. Tasaki, Prog. Theor. Phys. **99**, 489 (1998).
17 L. Ye, M. Kang, J. Liu, F. von Cube, C. R. Wicker, T. Suzuki, C. Jozwiak, A. Bostwick, E. Rotenberg, D. C. Bell, et al., Nature **555**, 638 (2018).
18 J. X. Yin, S. S. Zhang, H. Li, K. Jiang, G. Chang, B. Zhang, B. Lian, C. Xiang, I. Belopolski, H. Zheng, et al., Nature **562**, 91 (2018).
19 M. L. Kiesel, C. Platt, and R. Thomale, Phys. Rev. Lett. **110**, 126405 (2013).
20 W. S. Wang, Z. Z. Li, Y. Y. Xiang, and Q. H. Wang, Phys. Rev. B **87**,

115135 (2013).
21 L. Nie, K. Sun, W. Ma, D. Song, L. Zheng, Z. Liang, P. Wu, F. Yu, J. Li, M. Shan, et al., Nature **604**, 59 (2022).
22 X. Teng, L. Chen, F. Ye, E. Rosenberg, Z. Liu, J. X. Yin, Y. X. Jiang, J. S. Oh, M. Z. Hasan, K. J. Neubauer, et al., Nature **609**, 490 (2022).
23 C. Wu, D. Bergman, L. Balents, and S. Das Sarma, Phys. Rev. Lett. **99**, 070401 (2007).
24 E. Tang, J. W. Mei, and X. G. Wen, Phys. Rev. Lett. **106**, 236802 (2011).
25 K. Sun, Z. Gu, H. Katsura, and S. Das Sarma, Phys. Rev. Lett. **106**, 236803 (2011).
26 T. Neupert, L. Santos, C. Chamon, and C. Mudry, Phys. Rev. Lett. **106**, 236804 (2011).
27 Z. Lin, J. H. Choi, Q. Zhang, W. Qin, S. Yi, P. Wang, L. Li, Y. Wang, H. Zhang, Z. Sun, et al., Phys. Rev. Lett. **121**, 096401 (2018).
28 Z. Liu, M. Li, Q. Wang, G. Wang, C. Wen, K. Jiang, X. Lu, S. Yan, Y. Huang, D. Shen, et al., Nat. Commun. **11**, 4002 (2020).
29 M. Kang, S. Fang, L. Ye, H. C. Po, J. Denlinger, C. Jozwiak, A. Bostwick, E. Rotenberg, E. Kaxiras, J. G. Checkelsky, et al., Nat. Commun. **11**, 4004 (2020).
30 M. Kang, L. Ye, S. Fang, J. S. You, A. Levitan, M. Han, J. I. Facio, C. Jozwiak, A. Bostwick, E. Rotenberg, et al., Nat. Mater. **19**, 163 (2020).
31 S. A. Ekahana, Y. Soh, A. Tamai, D. Gosálbez-Martínez, M. Yao, A. Hunter, W. Fan, Y. Wang, J. Li, A. Kleibert, et al., Nature **627**, 67 (2024).
32 H. Huang, L. Zheng, Z. Lin, X. Guo, S. Wang, S. Zhang, C. Zhang, Z. Sun, Z. Wang, H. Weng, et al., Phys. Rev. Lett. **128**, 096601 (2022).
33 D. Di Sante, C. Bigi, P. Eck, S. Enzner, A. Consiglio, G. Pokharel, P. Carrara, P. Orgiani, V. Polewczyk, J. Fujii, et al., Nat. Phys. **19**, 1135 (2023).
34 Y. Hu, C. Le, Y. Zhang, Z. Zhao, J. Liu, J. Ma, N. C. Plumb, M. Radovic, H. Chen, A. P. Schnyder, et al., Nat. Phys. **19**, 1827 (2023).
35 Z. Zheng, L. Chen, X. Ji, Y. Zhou, G. Qu, M. Hu, Y. Huang, H. Weng, T. Qian, and G. Wang, Sci. China-Phys. Mech. Astron. **67**, 267411 (2024).
36 N. Regnault, Y. Xu, M. R. Li, D. S. Ma, M. Jovanovic, A. Yazdani, S. S. P. Parkin, C. Felser, L. M. Schoop, N. P. Ong, et al., Nature **603**, 824 (2022).
37 D. Călugăru, A. Chew, L. Elcoro, Y. Xu, N. Regnault, Z. D. Song, and B. A. Bernevig, Nat. Phys. **18**, 185 (2022).
38 M. Ochi, R. Arita, M. Matsumoto, H. Kino, and T. Miyake, Phys. Rev. B **91**, 165137 (2015).
39 T. N. Lamichhane, Q. Lin, V. Taufour, A. Palasyuk, T. Pandey, D. Parker, S. L. Budło, and P. C. Canfield, AIP Adv. **9**, 035138 (2019).
40 E. J. Monkman, C. Adamo, J. A. Mundy, D. E. Shai, J. W. Harter, D. Shen, B. Burganov, D. A. Muller, D. G. Schlom, and K. M. Shen, Nat. Mater. **11**, 855 (2012).
41 S. Sharma, A. Zintler, D. Günzing, J. Lill, D. M. Meira, R. Eilhardt, H. K. Singh, R. Xie, G. Gkouzia, M. Major, et al., ACS Appl. Mater. Interfaces **13**, 32415 (2021).
42 G. Kresse, and J. Hafner, Phys. Rev. B **47**, 558 (1993).
43 G. Kresse, and D. Joubert, Phys. Rev. B **59**, 1758 (1999).
44 J. P. Perdew, K. Burke, and M. Ernzerhof, Phys. Rev. Lett. **77**, 3865 (1996).
45 A. G. Petukhov, I. I. Mazin, L. Chioncel, and A. I. Lichtenstein, Phys. Rev. B **67**, 153106 (2003).
46 Y. Fang, Z. Wu, G. Yang, Y. Zhang, W. Zhu, Y. Wu, C. Guo, Y. Li, H. Yuan, J. X. Zhu, et al., Phys. Rev. B **108**, 125110 (2023).
47 P. D. C. King, H. I. Wei, Y. F. Nie, M. Uchida, C. Adamo, S. Zhu, X. He, I. Božović, D. G. Schlom, and K. M. Shen, Nat. Nanotech **9**, 443 (2014).
48 J. Maletz, V. B. Zabolotnyy, D. V. Evtushinsky, S. Thirupathaiah, A. U. B. Wolter, L. Harnagea, A. N. Yaresko, A. N. Vasiliev, D. A. Chareev, A. E. Böhmer, et al., Phys. Rev. B **89**, 220506 (2014).
49 S. Cheng, M. Nrisimhamurty, T. Zhou, N. Bagués, W. Zhou, A. J. Bishop, I. Lyalin, C. Jozwiak, A. Bostwick, E. Rotenberg, et al., Nano Lett. **23**, 7107 (2023).
50 H. Wu, C. Hu, Y. Xie, B. G. Jang, J. Huang, Y. Guo, S. Wu, C. Hu, Z. Yue, Y. Shi, et al., Phys. Rev. B **109**, 104410 (2024).
51 J. S. Kang, C. J. Yang, Y. P. Lee, C. G. Olson, E. J. Cho, S. J. Oh, R. O. Anderson, L. Z. Liu, J. H. Park, J. W. Allen, et al., Phys. Rev. B **48**, 10327 (1993).
52 J. D. Denlinger, J. W. Allen, J. S. Kang, K. Sun, B. I. Min, D. J. Kim, and Z. Fisk, in *Proceedings of the International Conference on Strongly Correlated Electron Systems (SCES2013)* (Tokyo, 2014) p. 017038.
53 A. Chikina, A. Generalov, K. Kummer, M. Güttler, V. N. Antonov, Y. Kucherenko, K. Kliemt, C. Krellner, S. Danzenbächer, T. Kim, et al., Phys. Rev. B **95**, 155127 (2017).
54 G. Kaindl, A. Höhr, E. Weschke, S. Vandré, C. Schüler-Langeheine, and C. Laubschat, Phys. Rev. B **51**, 7920 (1995).
55 D. Y. Usachov, D. Glazkova, A. V. Tarasov, S. Schulz, G. Poelchen, K. A. Bokai, O. Y. Vilkov, P. Dudin, K. Kummer, K. Kliemt, et al., J. Phys. Chem. Lett. **13**, 7861 (2022).
56 A. V. Tarasov, D. Glazkova, S. Schulz, G. Poelchen, K. Kliemt, A. Kraiker, M. Muntwiler, C. Laubschat, A. Generalov, C. Polley, et al., Phys. Rev. B **106**, 155136 (2022).
57 Z. P. Yin, K. Haule, and G. Kotliar, Nat. Mater **10**, 932 (2011).
58 R. Yu, and Q. Si, Phys. Rev. Lett. **110**, 146402 (2013).
59 S. Samanta, H. Park, C. Lee, S. Jeon, H. Cui, Y. X. Yao, J. Hwang, K. Y. Choi, and H. S. Kim, Nat. Commun. **15**, 5376 (2024).
60 J. Huang, L. Chen, Y. Huang, C. Setty, B. Gao, Y. Shi, Z. Liu, Y. Zhang, T. Yilmaz, E. Vescovo, et al., Nat. Phys. **20**, 603 (2024).
61 D. Givord, J. Laforest, J. Schweizer, and F. Tasset, J. Appl. Phys. **50**, 2008 (1979).
62 M. Kuz'min, and A. Tishin, Handb. Magn. Mater **17**, 149 (2007).
63 C. E. Patrick, S. Kumar, G. Balakrishnan, R. S. Edwards, M. R. Lees, L. Petit, and J. B. Staunton, Phys. Rev. Lett. **120**, 097202 (2018).
64 M. Mizumaki, S. Tsutsui, and F. Iga, J. Phys. Conf. Ser. **176**, 012034 (2009).
65 L. Li, K. Sun, C. Kurdak, and J. W. Allen, Nat Rev Phys **2**, 463 (2020).
66 F. Lu, J. Z. Zhao, H. Weng, Z. Fang, and X. Dai, Phys. Rev. Lett. **110**, 096401 (2013).
67 C. J. Kang, H. C. Choi, K. Kim, and B. I. Min, Phys. Rev. Lett. **114**, 166404 (2015).
68 D. Koudela, U. Schwarz, H. Rosner, U. Burkhardt, A. Handstein, M. Hanfland, M. D. Kuzłin, I. Opahle, K. Koepernik, K. H. Müller, et al., Phys. Rev. B **77**, 024411 (2008).
69 H. Rosner, D. Koudela, U. Schwarz, A. Handstein, M. Hanfland, I. Opahle, K. Koepernik, M. D. Kuz'min, K. H. Müller, J. A. Mydosh, et al., Nat. Phys. **2**, 469 (2006).
70 P. Coleman, Heavy Fermions: Electrons at the edge of magnetism. *Handbook of Magnetism and Advanced Magnetic Materials* (Wiley, New York, 2007).
71 P. Gegenwart, Q. Si, and F. Steglich, Nat. Phys. **4**, 186 (2008).
72 S. Kirchner, S. Paschen, Q. Chen, S. Wirth, D. Feng, J. D. Thompson, and Q. Si, Rev. Mod. Phys. **92**, 011002 (2020).
73 Y. Z. Zhao, J. J. Song, Q. Y. Wu, H. Liu, C. Zhang, B. Chen, H. Y. Zhang, Z. H. Chen, Y. B. Huang, X. Q. Ye, et al., Sci. China-Phys. Mech. Astron. **67**, 247413 (2024).
74 R. Xie, and H. Zhang, Phys. Rev. B **106**, 224411 (2022).
75 A. Galler, S. Ener, F. Maccari, I. Dirba, K. P. Skokov, O. Gutfleisch, S. Biermann, and L. V. Pourovskii, NPJ Quantum Mater. **6**, 2 (2021).
76 J. P. Wakefield, M. Kang, P. M. Neves, D. Oh, S. Fang, R. McTigue, S. Y. Frank Zhao, T. N. Lamichhane, A. Chen, S. Lee, et al., Nature **623**, 301 (2023).
77 J. G. Checkelsky, B. A. Bernevig, P. Coleman, Q. Si, and S. Paschen, Nat. Rev. Mater. **9**, 509 (2024).